Article

Molecularly resolved mapping of heterogeneous ice nucleation and crystallization pathways using in-situ cryo-TEM

Check for updates

Zibing Wang[1,2,8], Zifeng Yuan[3,8], Mouyang Cheng [3,8], Xudan Huang[1,2,8], Keyang Liu [3], Yihan Wang[4], Huacong Sun[1,2], Lei Liao[1,2], Zhi Xu[5], Ji Chen [3,6], Wenlong Wang [1,2,5], Lei Liu [4,6], Xuedong Bai [1,2,5] ✉, Limei Xu [3,6] ✉, Enge Wang [1,3,5,6,7] ✉ & Lifen Wang [1,2,5] ✉

Crystallization plays a fundamental role in diverse fields such as glaciology, geology, biology, and materials science. Among various crystallizing systems, the formation of ice remains elusive, despite decades of intensive investigation. In this study, we integrate in-situ cryogenic transmission electron microscopy with molecular dynamics simulations to develop a molecular-resolution mapping and thermodynamic framework for deposition freezing under low-temperature, low-pressure conditions. Our results demonstrate that ice formation on rapidly cooled substrates, representing far-from-equilibrium states, proceeds via an adsorption-mediated, barrierless pathway of heterogeneous ice nucleation, followed by progression toward thermo-dynamic equilibrium. This process is unveiled to involve a series of distinct yet interconnected steps, including amorphous ice adsorption, spontaneous nucleation and growth of ice I, Ostwald ripening, Wulff construction, oriented coalescence, and aggregation, all governed by interfacial free energy minima. Our findings offer direct molecular-level insight into the mechanisms of heterogeneous ice nucleation, enrich current understanding of non-classical nucleation pathways, and emphasize the critical role of interfacial energetics in shaping ice crystal morphology and quality.

The assembly of water molecules on foreign substrates, forming precipitation such as rain and snow, is a ubiquitous phenomenon that influences Earth's ecosystems and environments. Despite broad and intense research interests, the scenario of these heterogeneous nucleation and growth process remains far from well-understood. In the well-established ice phase diagram that present stable forms of ice at varied conditions, hexagonal ice, labeled as 'ice I' as the first discovered form, exhibits a hexagonal close-packed structure with

[1]Beijing National Laboratory for Condensed Matter Physics, Institute of Physics, Chinese Academy of Sciences, Beijing 100190, China. [2]School of Physical Sciences, University of Chinese Academy of Sciences, Chinese Academy of Sciences, Beijing 100190, China. [3]School of Physics, Peking University, Beijing 100871, China. [4]School of Materials Science and Engineering, Peking University, Beijing 100871, China. [5]Songshan Lake Laboratory for Materials Science, Dongguan 523000, China. [6]Interdisciplinary Institute of Light-Element Quantum Materials and Research Center for Light-Element Advanced Materials, Peking University, Beijing 100871, China. [7]Tsientang Institute for Advanced Study, Zhejiang 310024, China. [8]These authors contributed equally: Zibing Wang, Zifeng Yuan, Mouyang Cheng, Xudan Huang. ✉e-mail: xdbai@iphy.ac.cn; limei.xu@pku.edu.cn; egwang@pku.edu.cn; wanglf@iphy.ac.cn

rippled hexagons, where water molecules construct a tetrahedral arrangement through hydrogen bonding[1–3]. This form of ice is acknowledged as a final precipitation product and is commonly found in natural environments, exhibiting hexagonal symmetry. Despite its common occurrence, the water phase transition process, whereby water molecules assemble from the vapor or liquid phases into the hexagonal ice due to shifts in the environment conditions, remains a longstanding and fugitive focus in research[4–8].

In particular, the intricate microscopic details of ice formation remain elusive due to temporal and spatial challenges inherent in experiments[5,6,9–11]. Most crystallographic research methods, such as X-ray diffraction and neutron scattering, with the highest spatial resolution, are nonetheless prone to detecting homogeneous, uniform bulk structures due to their limited detection sensitivity. As a result, these methods lack dynamic information about the nucleation and growth processes that occur across length scales from microscopic to macroscopic. Environmental scanning electron microscopy offers a feasible approach for identifying active sites involved in heterogeneous ice formation[12,13], while water freezing assays enable direct observation of ice nucleation behavior in micrometer-sized single droplet and particles[14–18]. However, both techniques lack the spatial resolution required to capture the embryonic stages of ice nucleation at the molecular scale.

To bridge this gap, molecular dynamics (MD) simulations employing atomistic[19,20] and coarse-grained water models[21,22] have been widely employed to probe the microscopic mechanisms of ice formation. Among these, the monoatomic water (mW) model[23] has been extensively applied due to its computational efficiency and ability to reproduce key thermodynamic and structural properties of water, such as the melting point and local tetrahedrality[21,22,24,25], despite its limitations in representing hydrogen atoms and electrostatic interactions. Nevertheless, a comprehensive understanding of the microscopic crystallization pathway throughout the entire icing process, spanning from embryonic nucleation to the establishment of a thermodynamically stable phase, remains elusive. Whether the process follows a one-step classical nucleation theory[26,27], involves metastable intermediates as proposed in non-classical nucleation mechanisms[28], or proceeds via an adsorption-mediated nucleation pathway as recently suggested[29–31], remains an open question.

Here, by employing in-situ cryogenic transmission electron microscopy (cryo-TEM) with millisecond temporal resolution and picometer spatial resolution, we demonstrate a feasible experimental approach to directly map the microscopic crystallization pathways of ice I from nucleation to equilibrium states. These observations are further corroborated by MD simulations, demonstrating an amorphous ice adsorption-facilitated spontaneous nucleation and growth of polymorphic ice I during the vapor deposition process.

Results

Heterogeneous ice nucleation and growth

By the in-situ cryo-TEM equipped with high-resolution real-time and real-space imaging (see "Methods"), we investigated the microdynamics of ice I formation from vapor deposition on translucent graphene substrates under non-equilibrium conditions, with a temperature of 102 K and a pressure of 10^{-6} Pa. Figure 1 represents the process of crowded nucleation and growth, where multiple nuclei emerge within a relatively small region (Supplementary Movie 1). During the initial stages of vapor deposition (0–1 s), clusters of amorphous solid water[32,33] formed on the cryogenic graphene substrate, serving as an adsorption layer (Fig. 1a, b, f, g). This observation is consistent with the hypothesized adsorption nucleation theory for heterogeneous freezing in deposition mode[30].

Subsequently, two isolated hexagonal ice (ice Ih) nuclei, ≈5 nm in size and designated as Ih_1 and Ih_2, evidenced from the sequential TEM images and the respective corresponding fast Fourier transform (FFT)

data (Fig. 1c–e, h–j). From FFT, the diffraction peak corresponding to amorphous ice and estimated from the halo pattern was observed at 3.9 Å. This coincides with the position of the {100} Bragg peak of ice Ih with lattice constants of $a = 4.5$ Å and $c = 7.3$ Å. Both ice nuclei Ih_1 and Ih_1 were oriented in the ⟨001⟩ crystallography direction without lattice registry with the graphene substrate. The deposits during the initial nucleation process deduced from the real-time TEM images were not sharp-faceted and exhibited convex shapes.

While the ice Ih_2 nucleus gradually diminished and eventually disappeared, the nearby ice Ih_1 nucleus continued to grow (Fig. 1k, l), suggesting that either the larger size of the Ih_1 nucleus exceeds the critical size required for sustained growth, or that larger nuclei grow at the expense of smaller ones due to the Ostwald ripening process[34]. Meanwhile, a third hexagonal ice nucleus (Ih_3), a cubic-ice[35,36] twin nucleus (Ic_1), and a single-crystalline cubic ice nucleus (Ic_2) formed around ice Ih_1 nucleus (Fig. 1k–t). The corresponding FFT analysis of the sequential TEM images indicated that nucleus Ih_3 shared the same orientation as Ih_1 along the ⟨001⟩ crystallographic direction. In contrast, both Ic_1 and Ic_2 nuclei were oriented along the ⟨110⟩ axis, with {111} plane d-spacing of 2.3 Å, consistent with a face-centered cubic lattice constant of 6.4 Å. The competitive heterogeneous nucleation, growth, and aggregation of these ice deposits produced an evolving botryoidal shape, revealing surface instability driven by the diffusion of water molecules.

Both nuclei Ic_1 and Ic_2 first grew to a dozen nanometers in size in tens of seconds and then dissolved or sublimed finally without a notable solid-state phase transition (Fig. 1u–ad, Suppl. Figs. 1 and 2). As a corollary, we can declare that the transient ice Ic that observed during the crowded ice nucleation and growth process acted simply as a competitor for ice Ih. In parallel, ice Ih nuclei aggregated and grew to tens of nanometers (see more examples in Suppl. Figs. 3 and 4). This dynamic behavior indicated that a surface energy-minima driven ripening process was predominant, which might explain why the smaller-sized ice Ih_2 nucleus disappeared as the larger nuclei grew. In the following growth process, the randomly spread out ice clusters intuitively evolved towards the edge of the ice Ih island and aggregated (Fig. 1u–x). Finally, the initial convex ice Ih crystallite transformed into a 50-nm-sized well-formed euhedral crystallite in about an hour after the crowded growth, exhibiting a mature plate-like stout hexagonal prism (Fig. 1y).

Moreover, the corresponding FFT (Fig. 1ad) of the high-resolution TEM image of the ice crystallite clearly demonstrate the six prism facets of ice Ih, implying that Wulff's construction[37] in related to surface free energy was valid for the equilibrium crystal shape of ice Ih at microscopic size, consistent with the six-sided hexagonal crystal habit of ice I at macroscopic level.

Surface structure

The surface structure of the fully-grown ice Ih crystallite resulting from the crowded growth process was further carefully examined. Intriguingly, the exposed prism facets of the equilibrium ice Ih crystallite were partially coated with a thin layer of cubic ice, hinting at ice Ic nucleation occurred on this stable base (Fig. 2). Figure 2a shows the low-magnification TEM image of the faceted ice Ih crystallite. We sorted and numbered 12 typical ice crystallite areas in the micrograph. The corresponding TEM images of the respective regions were magnified and measured using the associated FFT (Fig. 2b).

Using the micro-domain lattice structure scanning analysis, we derived the planar spatial configuration of ice Ih crystallite, indicating that both the bulk and the upper sides of the hexagon (1–5) exhibited the structure of ice Ih oriented along the ⟨001⟩ crystallographic zone axis. Intriguingly, the other prism surfaces (6–12) featured an in-plane lattice epitaxial shell of ⟨111⟩ zone axis-oriented cubic ice measuring ≤ 1.5 nm in width, as evidenced by both micrographs and, notably, the corresponding FFT. In the FFT, the disappearance of diffraction spots
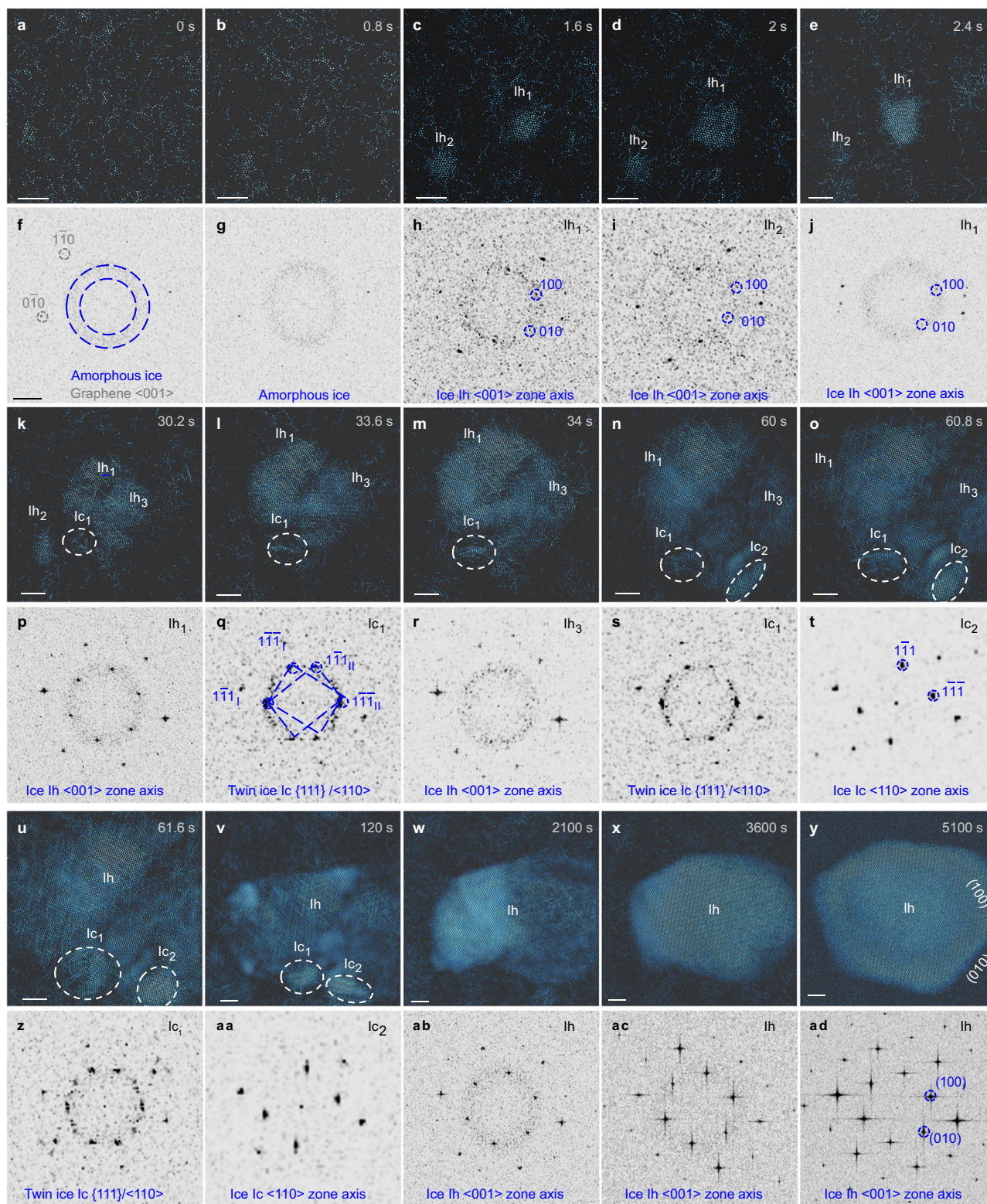
Fig. 1 | Heterogeneous ice nucleation and growth processes under low-temperature and low-pressure conditions. a–j Real-time TEM images of embryonic stages of ice deposition in top row (**a–e**) and the corresponding FFT of the image of nascent ice deposits in bottom row (**f, j**) showing amorphous ice deposition on the cryogenic graphene substrate first, followed by ⟨001⟩ crystallography direction-oriented hexagonal ice nucleation in the first few seconds. **k–t** In-situ TEM images and the corresponding FFT of the following nucleation process demonstrating that hexagonal ice (Ih₁) increased in size followed by

nucleation and growth of new nuclei (Ih₃) while Ih₂ gradually vanished, and two isolated ⟨110⟩-oriented cubic ice nuclei (Ic₁ and Ic₂) nucleated and grew to tens of nm in tens of seconds. **u–ad** Serial TEM images and the corresponding FFT of the crystal growth process, revealing that both cubic ice crystallites disappeared and hexagonal ice aggregated into a faceted crystallite with habit surface exposed. Scale bars: 5 nm in TEM images; 2 nm⁻¹ (shared) in the FFTs. TEM images are consistently displayed in blue color.
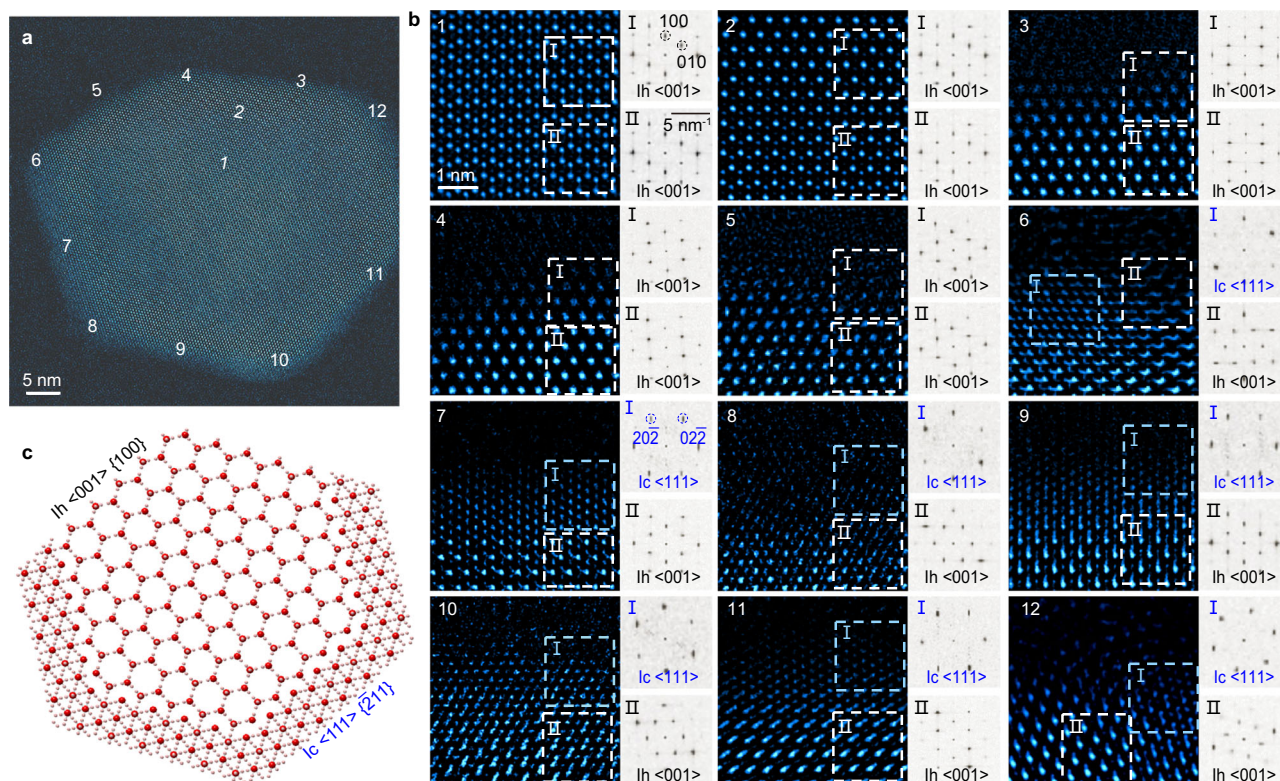
Fig. 2 | Surface structure of hexagonal ice grown at 100 K. a TEM image of a fully-grown hexagonal ice crystallite showing that faceted surfaces had a hexagon morphology. **b** High-magnification TEM images and the corresponding FFT of selected areas as numbered in (**a**), depicting hexagonal ice surface structure. **c** Illustration of the deduced hexagonal ice structure showing the ⟨001⟩ crystallography direction-oriented ice Ih crystallite partially wrapped by a ⟨111⟩-oriented ice Ic in the habit surface. TEM images are displayed in blue color. Scale bar for FFTs: 2 nm⁻¹ (shared across panels).

exclusively corresponding to {100} planes of ice Ih indicated a deviation of the structure in the shell from the bulk, leaving only spots representing {2$\bar{2}$0} planes for ice Ic, which were loosely distributed with a d-spacing of 2.3 Å (Fig. 2b, Suppl. Fig. 5). Accordingly, the observed mature crystallite displayed an intriguing in-plane Ih/Ic heterogeneous structure, as illustrated schematically in Fig. 2c.

Real-time images revealed the nucleation and growth of cubic ice on the prism surface of ice Ih crystallite during its faceting process. In contrast to the well-faceted mature ice Ih crystallite, the rounded ice Ih formed during the early stages of growth exhibited no signs of cubic ice on its surface (Suppl. Fig. 6). This suggests that the probabilistic nucleation of ice Ic under current conditions does not transition to the thermodynamically stable ice Ih, indicating that it is not an intermediate phase in the nucleation and growth pathway of ice Ih. More intriguingly, the region where the cubic ice shell was discovered corresponded to the lower portion of ice Ih, where previous observations have noted the nucleation and dissolution of ice Ic crystallites. In stark difference, the cubic ice shell was oriented in ⟨111⟩ direction that is distinct from the ⟨110⟩ orientation for the initial Ic crystallites. It is noteworthy that the {11$\bar{2}$} planes of ⟨111⟩-oriented ice Ic aligned with the {100} planes of ⟨001⟩-oriented ice Ih, demonstrating an unexampled in-plane coherent heterostructure. Thus, these observed coincidences suggest that the unusual cubic shell forming on the ice Ih structure might have resulted from growth driven by interfacial free energy minima.

Oriented aggregation

It is evident that the interplay between nuclei polytype, interface orientation, nuclei size, and nuclei spacing resulted in varied growth patterns of ice crystallites in the present conditions. Further observations suggested that when concomitant polymorphic ice nuclei were spaced slightly farther apart and grew

independently, cubic ice achieved sizes similar to those of equilibrium ice Ih via a comparable process of nucleation, aggregation, and faceting (Suppl. Figs. 7 and 8). More intriguingly, when the sizes of polymorphic ice nuclei were similar, and the distance between them was within the nanometer range (Fig. 3), the orientation-aligned polymorphs, albeit occasionally happening, tended to form a coherent interface as they grew and attached. This further supports the critical role of interfacial free energy minima-driven oriented aggregation in dictating ice growth. Figure 3a, b shows that a ⟨001⟩ zone axis-oriented ice Ih nuclei first formed in the amorphous ice matrix and then grew to several nanometers on a graphene substrate. Later on, the growth of this ice Ih nuclei was followed by the nucleation and growth of a ⟨111⟩ zone axis-oriented ice Ic crystallite (Fig. 3c–l).

Analysis of the FFTs corresponding to sequential micrographs showed that the two polymorphic nuclei aligned in the layer-stacking direction orientation from the embryonic nucleation stage (Fig. 3e–h, m–p). Moreover, the basal {110} plane of the ⟨001⟩ crystallography direction-oriented ice Ih nucleus and the {2$\bar{2}$0} plane for the ⟨111⟩ crystallography direction-oriented ice Ic were found to be parallel. Consequently, when the two polymorph ice nuclei grew and attached, the resulting fused hexagons once again formed an in-plane coherent heterojunction (Fig. 3k). It seems that this in-plane heterogeneous configuration has been overshadowed by the out-of-plane heterostructures found in ice Isd, which have drawn more attention in previous discussions[7,38]. However, the growth dynamics revealed here suggest that it is plausible for both types of heterostructures to form during ice growth driven by coherent interfaces.

The oriented assembly and faceting phenomena observed in the present study are consistent with growth processes reported in other systems, such as mesocrystals and inorganic crystals[39].
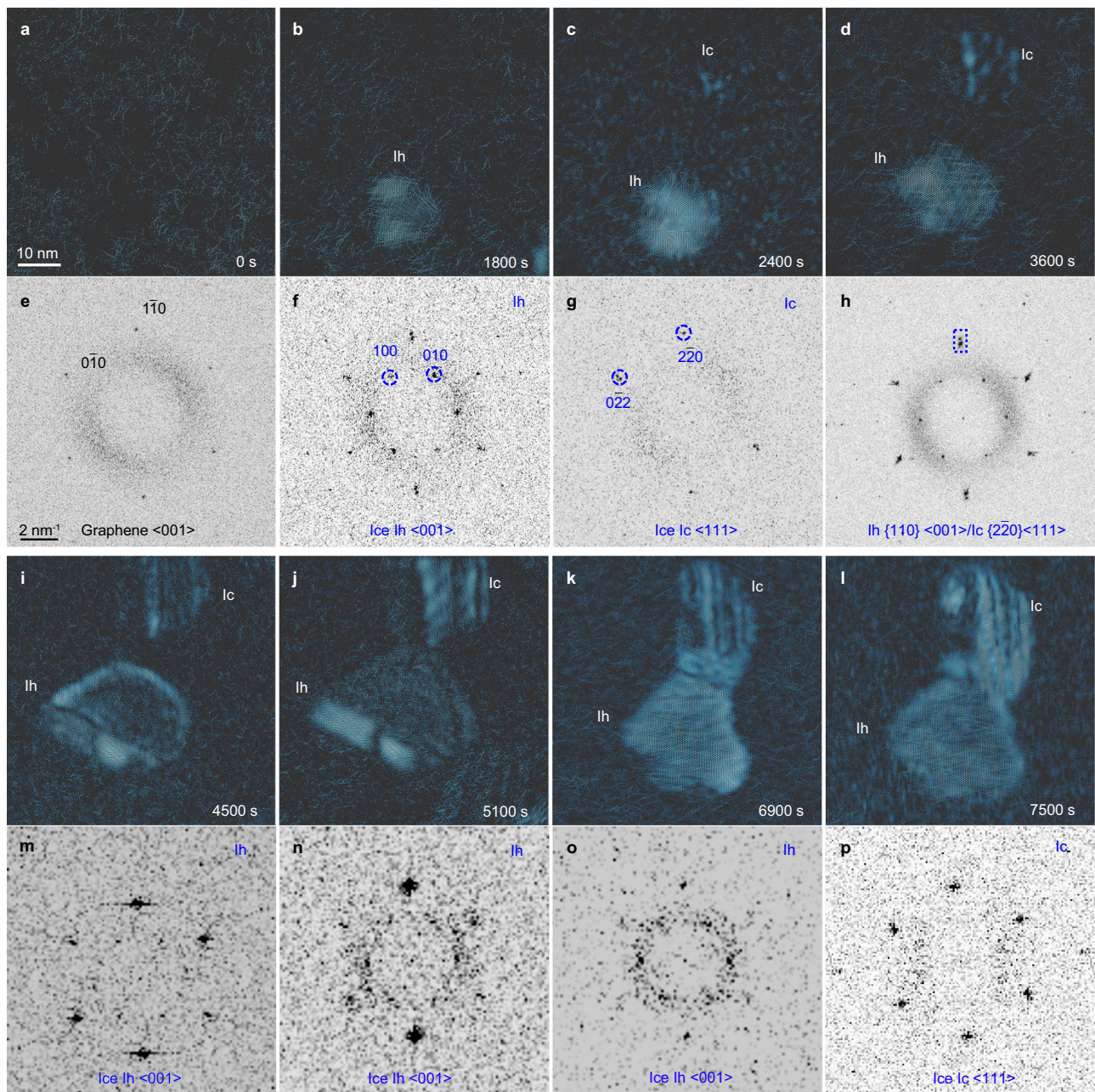
Fig. 3 | Concomitant polymorphic ice I nucleation and aggregation into an in-plane heterostructure. a–h Time-lapsed TEM images and the corresponding FFT of the embryonic stages of heterogeneous ice nucleation showing amorphous ice first deposited on graphene, followed by ice Ih nucleation in tens of minutes, and then by nucleation and growth of cubic ice nucleus oriented along the ⟨111⟩ zone axis, with the {2$\bar{2}$0} plane aligned with the {110} crystal plane of hexagonal ice. **i–p** In-situ sequential TEM images and selected area FFT of the nuclei showing growth into an in-plane heterostructure without notable transformation. TEM images are presented in blue color. The scale bar in **a** is shared across all TEM image panels, while the scale bar in **e** is shared across all FFT panels.

This reaffirms the significance of interface engineering in crystal assembly within the context of ice formation. The concept of oriented interface-driven aggregation might reveal why macro-sized snowflakes consistently exhibit a sixfold rotational symmetrical self-similar fractal structure that aligns with their microscopic symmetry, despite the assembly of numerous branches during the growth process.

Spontaneous nucleation

While the microscopic ice growth data supports the validity of thermodynamic criteria based on free energy minima, the complex polymorphism resulting from the probabilistic presence of metastable cubic ice observed here is challenging to explain, warranting a detailed study into the critical nucleation stages. The CNT indicates that the nuclei directly enter the stable phase when they exceed the critical size as to overcome the free energy barrier[27]. Recent investigations on kinetics in biomineralizations demonstrated that the crystallization passes through less stable states to finally reach the most stable crystalline state, i.e., following the Ostwald's law of phases[40]. The anomaly of the observed ice nucleation pathway in the present study thus suggests that ice Ic could have been only a transient intermediate phase in previously established models based on the fact that ice Ic is considered metastable compared to ice Ih[32]. The consistently observed ice Ic either nucleates and grows independently or nucleates over on mature Ih crystallites, suggesting that the process for polymorphic ice nucleation is a stochastic selection other than a thermodynamic

preference dictated by the free-energy landscape under the current conditions as illustrated in Fig. 4a.

To gain a deeper understanding of the nucleation process, we conducted a statistical analysis of heterogeneous ice nucleation and growth rates under the present conditions by tracking a large number of individually ice nuclei as they formed. The entire process, from the embryonic to the equilibrium state of over 100 groups of isolated nucleated nuclei, was meticulously recorded. The corresponding large-scale nucleation and growth processes were charted. Several sequential TEM imaging recording examples are depicted in Suppl. Fig. 9. Figure 4b presents scattered plots of growth rates against the radius size of nuclei throughout the entire growth process. Instantaneous growth rates were calculated based on raw experimental data because the nucleation and growth rates measured in our system rapidly decay over time and reach various plateaus (Fig. 4c, d). In contrast to the classical nucleation scenario where nuclei smaller than a critical size tend to shrink, it is evident that there was a consistent statistical increase in the sizes of ice nuclei observed in the present study.

Additionally, the net growth probabilities for ice nuclei throughout the overall growth process were consistently positive (Fig. 4e). This observation suggests the absence of a critical nucleus size, r_c, which lies within the range where the net probability changes from negative to positive, as predicted by CNT. Alternatively, this implies a zero free-energy barrier within the framework of CNT, leading to spontaneous ice nucleation in the current conditions.

The initial average growth rate was estimated to be $\dot{G} = 4.7 \times 10^{-2}$ nm s^{-1}, while the nucleation rate was $\dot{N} = 4.6 \times 10^{7}$ cm^{-2}s^{-1} (see "Methods"), surpassing previous studies in heterogeneous nucleation for the supercooled water regime around 250 K in the atmosphere by at least three to four orders of magnitude[4]. Given the significant differences between the current and atmospheric conditions, the absence of empirical parameters within this gap presents considerable challenges when extrapolating heterogeneous ice nucleation models from the atmosphere to this extreme environment.

We extended CNT, which is based on atmospheric parameters, to low-temperature environments for the analysis of heterogeneous nucleation in extremely supercooled conditions, identifying free energy barriers despite limitations such as the lack of microscopic description and the failure of capillarity approximation in early and strong supercooling stages (see "Methods"). Nonetheless, CNT offers qualitative insights into thermodynamics and kinetics across various systems, extending its applicability from gas-liquid to gas-solid transitions, including heterogeneous nucleation[4,9]. Assessing the nucleation free energy barrier across temperatures ranging from mild to deeply strong supercooling states relative to the melting temperature of 269 K, the observed energy barrier in the mild supercooling state aligned with previously reported values[41], confirming the reliability of the parameters used in the study (see "Methods", Suppl. Fig. 10).

Consequently, the determined energy barrier was approximately 0.22 kT under the present supercooled vapor deposition conditions. With this barrier lower than 1 kT, ice nucleation became spontaneous as thermal perturbation aided in overcoming the barrier, consistent with experimental statistical data. This spontaneous nucleation behavior of randomly-oriented, polymorphic ice I was also observed on hBN and amorphous carbon substrates (Suppl. Figs. 11 and 12), implying that under deeply supercooled conditions, which are characterized by reduced kinetic energy and dominant hydrogen-bonding interactions, heterogeneous ice nucleation proceeds via a similar mechanism regardless of the specific substrate. In other words, both experimental and computational data suggest that the current state of deep supercooling will lead to energy-barrier-free heterogeneous nucleation of cubic and hexagonal phases. This, in turn, results in the formation of various polymorphs and heterojunction structures through subsequent growth processes, driven by the lowest interface energy.

Non-classical growth

MD simulations were conducted to further evaluate the free energy profile for the nuclei growth pathways observed in the experiments, including discrete growth, oriented aggregation, and Ostwald ripening, as shown in Fig. 5 (see "Methods", Supplementary Fig. 13). Specifically, we investigated the growth and ripening of three typical ice nuclei with Ih⟨001⟩, Ic⟨111⟩, and Ic⟨110⟩ orientations exposed to the substrate, which are the predominant ice structures observed experimentally and exhibit the lowest potential energy in MD simulations (Suppl. Fig. 14). Figure 5a presents the MD snapshots and the corresponding free energy profile for the growth of ice Ic and Ih nuclei growth through monomer attachment, demonstrating a rapid decrease in free energy that indicates a preference for discrete growth in the initial stages. Figure 5b–e illustrates the typical merging process of nuclei during growth. Ice Ic along the ⟨110⟩ orientation tends to form twin boundaries on the {111} stacking planes, resulting in varied twin crystals, while ice Ih undergoes oriented aggregation upon contact, highlighting the interfacial-driven growth process. This behavior is also observed in the merging of polymorphic nuclei as shown in Fig. 5e, where larger ice Ih tend to consume smaller ice Ic nuclei, indicating a ripening process. Additionally, larger ice Ih can also consume smaller ice Ih as well. When nuclei of comparable sizes come into contact, the resulting heterostructure of ice Ic and ice Ih with a coherent interface exhibit a metastable state to a single-phase crystal.

The overall free energy evolution pathway for the competitive growth of ice Ic and ice Ih nuclei was further examined. Figure 5f presents a plausible pathway that illustrates discrete growth through monomer attachment during the initial stages. Upon contact between two or more nuclei, the interfacial-driven merging process causes a reduction in free energy, resulting in the formation of stable crystalline phases. It is noteworthy that the interfacial-driven coalesce scenario demonstrates lower free energy and greater efficient compared to discrete growth, providing mechanistic support for the experimentally observed post-nucleation phenomena.

In the future, further studies on ice crystallization dynamics under varying environmental conditions are crucial to fully reveal the microscopic kinetic nucleation pathways underling the thermodynamic phase diagram, as well as to gain a deeper understanding of the phase transitions and critical phenomena in ice. Moreover, experimentally examining the microscopic mechanisms serves to furnish empirical parameters that are essential for a foundational understanding in harmony with theoretical concepts of nucleation kinetics and thermodynamics. This symbiotic relationship between empirical and theoretical research facilitates a more profound understanding of the prevalent crystallization process, holding promise for guiding crystal design and optimizing performance.

Methods

In-situ cryogenic TEM characterization

An ultra-low dose in-situ cryogenic TEM imaging technique[36] was employed to visualize the formation and growth process of individual ice I crystallites on monolayer graphene substrates at molecular resolution. Residual water vapor in the high vacuum (≈10^{-6} Pa) of a TEM column served as the precursor source while the temperature gradually cooled from room temperature to ≈100 K over the course of 30 min. Solid state water deposition was initiated in low-pressure conditions when the temperature dropped to 110 K, which was consistent with previous observations.

Data fitting

Individual ice nuclei were monitored in real time to observe the nucleation and growth processes. The time-dependent behavior of ice nucleation and growth was elucidated using the Avrami equation[42],
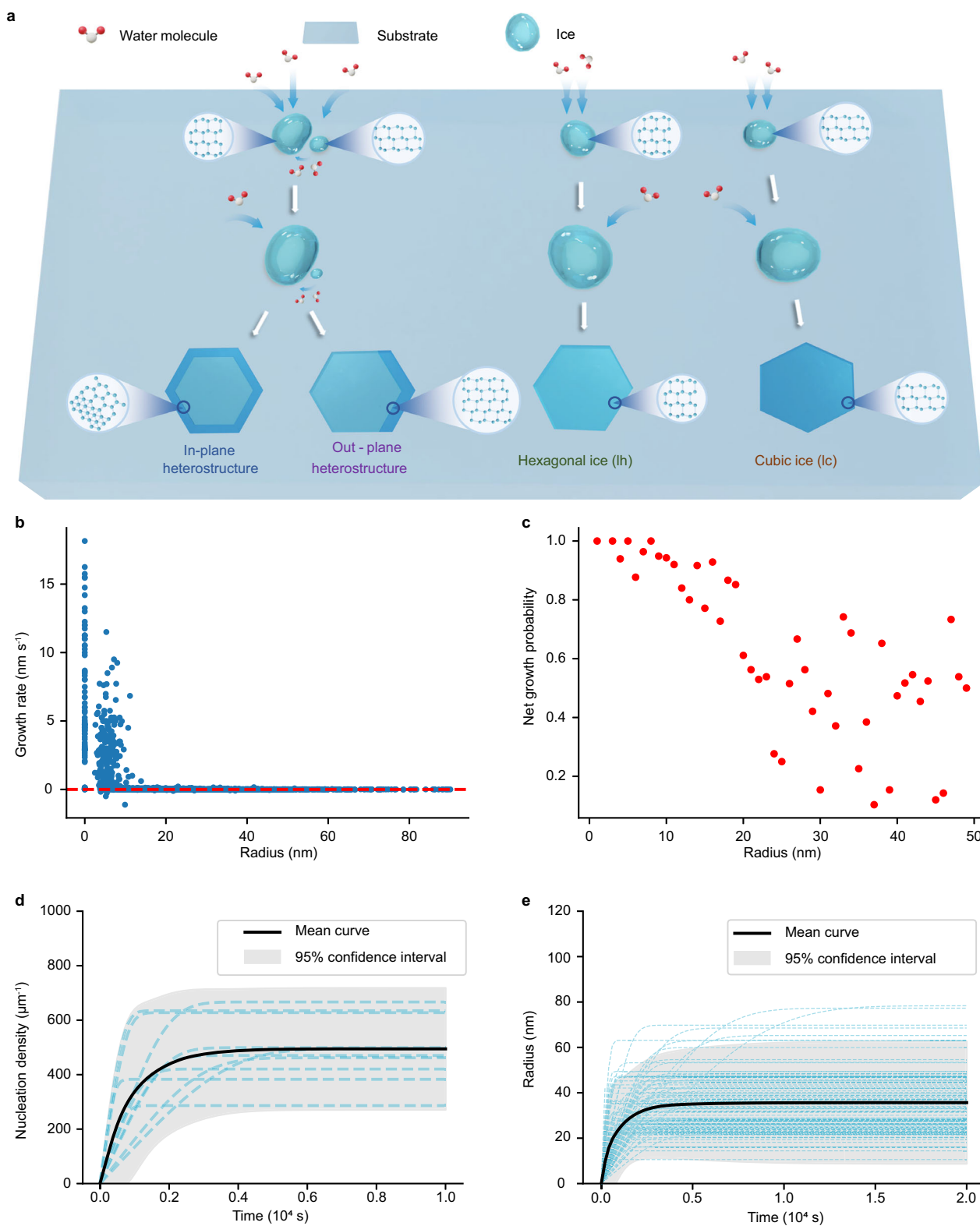
Fig. 4 | Statistical analysis of heterogeneous ice nucleation data. a Schematic illustration of the nucleation and crystallization pathways, including crowded nucleation and growth induced formation of in-plane and out-of-plane Ih/Ic heterostructures, along with independent nucleation and growth of hexagonal ice and cubic ice. **b** Instantaneous growth rates plotted against the size of 100 individual ice nuclei sampled across multiple time frames. **c** Plot of net growth possibility against the radius of 100 individual ice nuclei, revealing a consistent positive growth trend across all samples. Net growth possibility is defined as the difference in probability between an ice nucleus increasing and decreasing in size. Evolution of **d** nucleation number density and **e** nucleus size versus time. In both plots, each dashed colored line shows fitting for an individual measurement, while the average results are plotted using solid black lines. The shaded region indicates the 95% confidence interval.
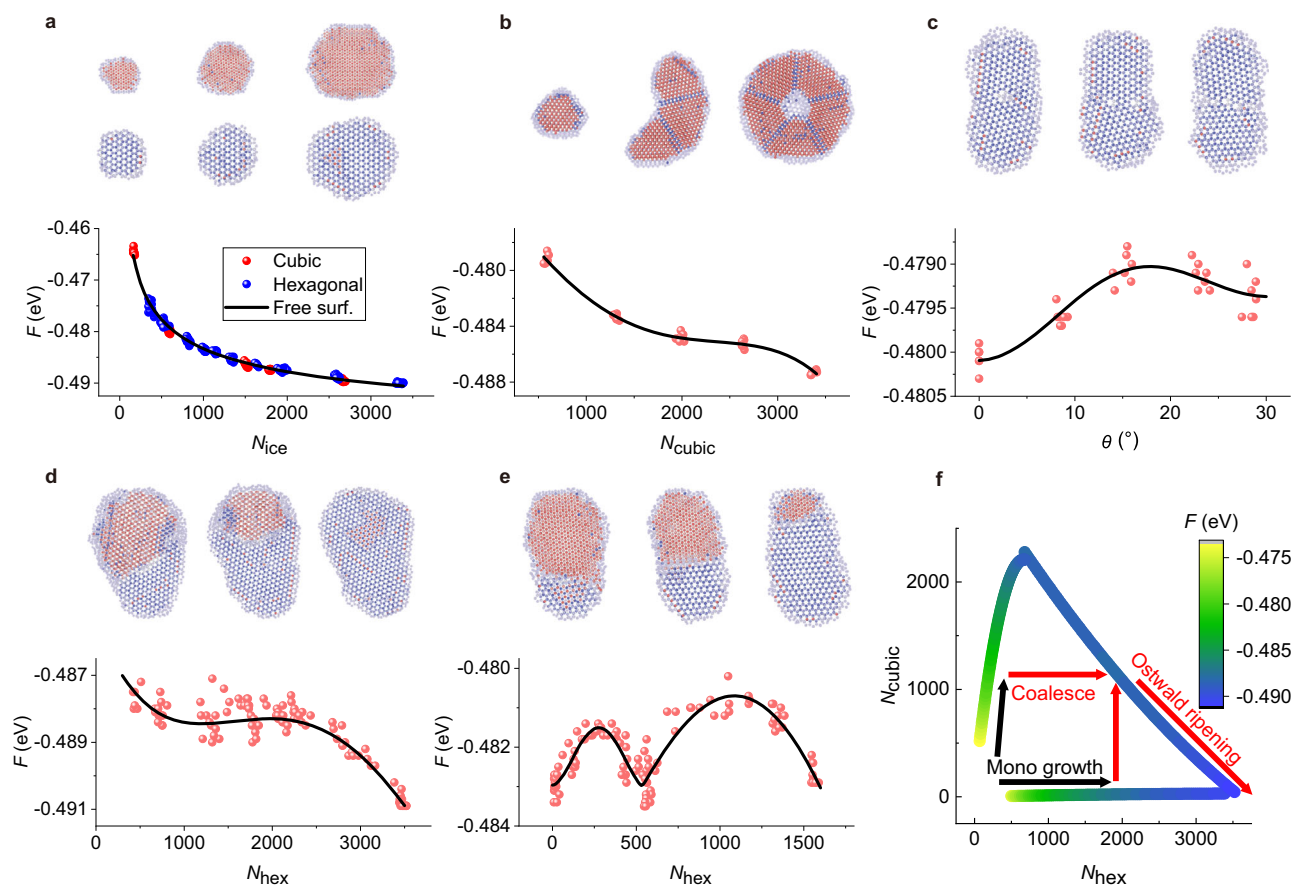
Fig. 5 | Free energy profiles for ice growth. a Molecular dynamics simulation snapshots illustrate the growth evolution of cubic ice and hexagonal ice through monomer attachment, accompanied by the corresponding free energy surface profile, demonstrating that free energy per water molecule decreases with increasing molecular number. **b** MD snapshots and the corresponding free energy profile illustrate the aggregation of cubic ice ⟨110⟩ along the ⟨111⟩ direction, featuring twin boundaries that produce a stable five-fold symmetry structure. **c** Aggregation of hexagonal ice nuclei, showing oriented aggregation with grain rotation, ultimately achieving a zero-degree orientation angle in the final stable state. **d** Merging of ice Ih ⟨001⟩ and one smaller sized ice Ic ⟨110⟩, showing growth of hexagonal ice nuclei. **e** Merging of Ih ⟨001⟩ and Ic ⟨111⟩ nucei as a function of the size of ice Ih reveals three free energy minima and two energy barriers, indicating that one nucleus grows at the expense of the other, with one metastable state characterized by coalescence at a coherent interface between the Ih and Ic nuclei. **f** Summary of the free energy evolution pathways for the cooperative growth of Ih and Ic nuclei shows an initial discrete growth path, followed by interfacial-driven coalescence and ripening.

which describes transition kinetics from one phase to another via random formation of nuclei in the parent phase[43]. We fitted the following equations to the experimental nucleation density $n(t)$ and nuclei size $r(t)$ data by modifying the original Avrami equation:

$$\frac{dn}{dt} = \dot{N}e^{-(t/t_1)^3} \qquad (1)$$

$$\frac{dr}{dt} = \dot{G}e^{-(t/t_2)^3} \qquad (2)$$

The exponential decay over t^3 arises from the finite volume effect on a two-dimensional plane, while the nucleation rate $\dot{N}$ and growth rate $\dot{G}$ represent the maximum rates at the initial time.

We first performed such fitting for each individual data curve to smoothen the fitted results and then plotted the average smoothed $n(t)$ and $r(t)$ over all samples. Next, we extracted the initial nucleation and growth rates from the smoothed $n(t)$ and $r(t)$ using the finite-difference method.

Second-order corrections included ΔG estimation
Second-order corrections to thermodynamic parameters were introduced into the computation of Gibbs free energy to better capture the

thermodynamics of water-ice transition[44]. The equation for ΔG is given by

$$\Delta G = \frac{16\pi T_m^2 v_{ice}^2 \gamma_{sl}^3}{3(\Delta H_m)^2 (\Delta T)^2} - \frac{8\pi T_m^2 v_{ice}^2 \Delta C \gamma_{sl}^3}{3(\Delta H_m)^3 \Delta T} \qquad (3)$$

where v_{ice} is the molecular volume of ice (3.165×10^{-29} m³), ΔC is the difference in isobaric heat capacity between water and ice (40.1 J mol⁻¹ K⁻¹) (ref. [45]), ΔH_m is the enthalpy change from water to ice (5.01 kJ mol⁻¹), and ΔT refers to supercooling (167 K)[46], while the melting temperature is 269 K. Experimental data for ΔC suggest values around 40.1 J mol⁻¹ K⁻¹ (ref. [45]), while calculations for TIP4P/2005 yielded a value close to 41.8 J mol⁻¹ K⁻¹ (ref. [47]). Enthalpy data for ice and water at various temperatures provide a value of 39.4 J mol⁻¹ K⁻¹ (ref. [44]). Surface tension is estimated at 26.2 mJ mol⁻¹ (ref. [44]): a value between 30.88 mJ mol⁻¹ for Ih/water and 23.65 mJ mol⁻¹ for Ic/water[46].

The estimated barriers were in good agreement with the findings by Niu et al.[41] and Wang et al.[44] in mild supercooling conditions. This method also serves as a useful test for CNT in strong supercooling conditions.

Two sets of parameters were employed to describe the nucleation barrier from vapor to ice in strong supercooling conditions. In the more precise set of parameters, ΔH_{sv} was calculated as the sum of ΔH_{sl}

at 273 K and ΔH_{lv} at 273 K, resulting in $(6.017 + 45.064)$ kJ mol^{-1} = 51.081 kJ mol^{-1} (ref. [48]). Additionally, a numerical fit of ice enthalpy and vapor enthalpy in mild supercooling conditions was used to extrapolate ΔH_{sv} during strong supercooling. Specifically, the extrapolated ΔH_{sv} was found to be 51.344 kJ mol^{-1} at the experimental temperature of 102 K and remained relatively stable (0.6% change) within the range of 98–273.15 K.

Regarding ΔC_p, a significant variation was observed in the reported estimates of isobaric heat capacity for water, with reported values of 75.730 J mol^{-1} K^{-1} (273.15 K)[49], 76.023 J mol^{-1} K^{-1} (273.15 K)[48], 99 J mol^{-1} K^{-1} (273.15 K)[44], and 117.152 J mol^{-1} K^{-1} (235 K)[49]. The values for ice were 13.141 J mol^{-1} K^{-1} (102 K)[48], 37.97 J mol^{-1} K^{-1} (273.15 K)[48], to 59.6 J mol^{-1} K^{-1} (273.15 K)[44]. In addition, a value of 16.033 J mol^{-1} K^{-1} at 100 K has been reported for vapor[48].

Conversely, surface tension is challenging to measure, with reported values of 10 and 44 mJ m^{-2} at the melting temperature[50]. Typically, it can only be determined indirectly using the Young's equation, which involves known contact angles of liquid on solid and known surface tensions[51]. In the present calculations, 59.6 J mol^{-1} K^{-1} was directly utilized as ΔC_p and 75.7 mJ m^{-2} as the surface tension.

The following liquid-like values were adopted in the alternate set of parameters: 23.65 mJ m^{-2} for the surface tension[46], 5.01 kJ mol^{-1} for the enthalpy change[46], 59.6 J mol^{-1} K^{-1} for the change in isobaric heat capacity[44], and 269 K for the melting temperature[46].

Ice saturation ratio included ΔG estimation

Using saturation ratio[52] is another method to estimate ΔG, such that

$$\Delta G = \frac{16\pi T_m^2 v_{ice}^2 \gamma_{sl}^3}{3(kT\ln S)^2} \tag{4}$$

The molecular volume of ice and surface tension remain the same as described above. The ice saturation ratio (S) is defined as the ratio between the vapor pressures of supercooled vapor and ice. Our experimental vapor pressure (10^J Pa) was utilized in the present study and the parameterizations for the vapor pressure of ice were employed according to the following equations described by Murphy and Koop[52,53]:

$$\ln(P_{ice}) = 9.550426 - \frac{5723.265\,K}{T} + 3.53068\ln T - 0.00728332 K^{-1} T \tag{5}$$

and $S = \frac{P_{vapor}}{P_{ice}}$, where T and p are in K and Pa, respectively. Numerical differences were observed between the results obtained using the two methods. However, the qualitative conclusion of spontaneous nucleation was indicated by both as the barriers were smaller than $1\,kT$.

Molecular dynamics simulations

To model the evolution and coalesce of cubic and hexagonal ice nuclei on graphene substrate, we perform molecular dynamics simulations using the large-scale atomic or molecular massively parallel simulator (LAMMPS) package[54]. The water–water interaction is modeled by the monatomic water model mW[23]. The graphene substrate is modeled as either (i) a structureless flat wall interacting with water via a 9-3 Lennard–Jones (LJ) potential with $\varepsilon_{sub} = 1.7$ kcal mol^{-1} and $\sigma_{sub} = 0.356$ nm (ref. [24]), or (ii) an atomistic multilayer graphene slab, where water–carbon interactions are described by a two body Stillinger-Weber potential with $\sigma = 0.32$ nm and $\varepsilon = 0.13$ kcal mol^{-1} consistent with previous work[24]. The cutoff radius was set to $r_c = 2.5\sigma_{sub}$. These values yield water contact angles consistent with those measured on graphitic surfaces (≈80°). The carbon atoms in the graphene slabs were kept frozen during the simulations, and therefore no intralayer carbon–carbon potential was applied. A 10 nm vacuum slab was added in the z direction perpendicular to the xy plane of

graphene substrate. The Nosé–Hoover thermostat is used to maintain the temperature, with a thermostat relaxation time of 0.1 ps. The equations of motion for the water molecules were integrated with a time step of 1 fs. The initial states of cubic and hexagonal ice nuclei are separately created by the GenIce2 software[55] and then fully relaxed on the graphene substrate. The coalesce process are thus simulated by placing two ice nuclei on one substrate at a distance of several Å.

To promote the structural transformation and relaxation during the coalesce process, a thermal cycling[56] is applied with repetitive heating and cooling of the ice nuclei. Ice nuclei were thermally cycled between 100 and 230 K, with heating and cooling durations of 0.6 ps and 0.4 ps, respectively (see Suppl. Fig. 15 for the full temperature protocol). Potential energy and ice configurations were monitored during the cycles to ensure convergence of both structure and energy for at least 10 cycles prior to the end of the simulation. The intermediate and final structures during the coalesce process are extracted at the cooling stage to compute the free energy of these structures. The free energy of the ice nuclei configurations is computed by the thermodynamic integration methods[57] with the Frenkel–Ladd path[58].

Data availability

The data that support the findings of this study are available from Figshare[59] and from the corresponding authors upon request.

References

1. Bernal, J. D. & Fowler, R. H. A theory of water and ionic solution, with particular reference to hydrogen and hydroxyl ions. *J. Chem. Phys.* **1**, 515–548 (1933).
2. Barnes, W. H. & Bragg, W. H. The crystal structure of ice between 0 °C. and —183 °C. *Proc. R. Soc. Lond. Ser. A* **125**, 670–693 (1929).
3. Pauling, L. The structure and entropy of ice and of other crystals with some randomness of atomic arrangement. *J. Am. Chem. Soc.* **57**, 2680–2684 (1935).
4. Knopf, D. A. & Alpert, P. A. Atmospheric ice nucleation. *Nat. Rev. Phys.* **5**, 203–217 (2023).
5. Bauer, R., Tse, J. S., Komatsu, K., Machida, S. & Hattori, T. Slow compression of crystalline ice at low temperature. *Nature* **585**, E9–E10 (2020).
6. Tulk, C. A., Molaison, J. J., Makhluf, A. R., Manning, C. E. & Klug, D. D. Absence of amorphous forms when ice is compressed at low temperature. *Nature* **569**, 542–545 (2019).
7. Lupi, L. et al. Role of stacking disorder in ice nucleation. *Nature* **551**, 218–222 (2017).
8. Takahashi, T. On the role of cubic structure in ice nucleation. *J. Cryst. Growth* **59**, 441–449 (1982).
9. Sosso, G. C. et al. Crystal nucleation in liquids: open questions and future challenges in molecular dynamics simulations. *Chem. Rev.* **116**, 7078–7116 (2016).
10. Matsumoto, M., Saito, S. & Ohmine, I. Molecular dynamics simulation of the ice nucleation and growth process leading to water freezing. *Nature* **416**, 409–413 (2002).
11. Reinhardt, A. & Doye, J. P. K. Free energy landscapes for homogeneous nucleation of ice for a monatomic water model. *J. Chem. Phys.* **136**, 054501 (2012).
12. Kiselev, A. et al. Active sites in heterogeneous ice nucleation—the example of K-rich feldspars. *Science* **355**, 367–371 (2017).
13. Wang, B. et al. Direct observation of ice nucleation events on individual atmospheric particles. *Phys. Chem. Chem. Phys.* **18**, 29721–29731 (2016).
14. Lee, J. C., Hansen, T. & Davies, P. L. Droplet freezing assays using a nanoliter osmometer. *Cryobiology* **113**, 104584 (2023).
15. Häusler, T., Witek, L., Felgitsch, L., Hitzenberger, R. & Grothe, H. Freezing on a chip—a new approach to determine heterogeneous ice nucleation of micrometer-sized water droplets. *Atmosphere* **9**, 140 (2018).

16. Tobo, Y. An improved approach for measuring immersion freezing in large droplets over a wide temperature range. *Sci. Rep.* **6**, 32930 (2016).

17. Whale, T. F. et al. A technique for quantifying heterogeneous ice nucleation in microlitre supercooled water droplets. *Atmos. Meas. Tech.* **8**, 2437–2447 (2015).

18. Vali, G. Quantitative evaluation of experimental results an the heterogeneous freezing nucleation of supercooled liquids. *J. Atmos. Sci.* **28**, 402–409 (1971).

19. Zhang, Y. et al. Fully atomistic molecular dynamics simulation of ice nucleation near an antifreeze protein. *J.Am. Chem. Soc.* **147**, 4411–4418 (2025).

20. Shao, M. et al. Hydrogen polarity of interfacial water regulates heterogeneous ice nucleation. *Phys. Chem. Chem. Phys.* **22**, 258–264 (2020).

21. Lupi, L., Hudait, A. & Molinero, V. Heterogeneous nucleation of ice on carbon surfaces. *J. Am. Chem. Soc.* **136**, 3156–3164 (2014).

22. Davies, M. B., Fitzner, M. & Michaelides, A. Routes to cubic ice through heterogeneous nucleation. *Proc. Natl Acad. Sci. USA* **118**, e2025245118 (2021).

23. Molinero, V. & Moore, E. B. Water modeled as an intermediate element between carbon and silicon. *J. Phys. Chem. B* **113**, 4008–4016 (2009).

24. Lupi, L., Kastelowitz, N. & Molinero, V. Vapor deposition of water on graphitic surfaces: Formation of amorphous ice, bilayer ice, ice I, and liquid water. *J. Chem. Phys.* **141**, 18C508 (2014).

25. Fitzner, M., Sosso, G. C., Cox, S. J. & Michaelides, A. The many faces of heterogeneous ice nucleation: interplay between surface morphology and hydrophobicity. *J. Am. Chem. Soc.* **137**, 13658–13669 (2015).

26. Cabriolu, R. & Li, T. Ice nucleation on carbon surface supports the classical theory for heterogeneous nucleation. *Phys. Rev. E* **91**, 052402 (2015).

27. Gibbs, J. W. On the equilibrium of heterogeneous substances. *Trans. Connect. Acad. Sci.* **16**, 441–458 (1878).

28. Russo, J., Romano, F. & Tanaka, H. New metastable form of ice and its role in the homogeneous crystallization of water. *Nat. Mater.* **13**, 733–739 (2014).

29. Roudsari, G., Lbadaoui-Darvas, M., Welti, A., Nenes, A. & Laaksonen, A. The molecular scale mechanism of deposition ice nucleation on silver iodide. *Environ. Sci.* **4**, 243–251 (2024).

30. Lbadaoui-Darvas, M., Laaksonen, A. & Nenes, A. Deposition freezing, pore condensation freezing and adsorption: three processes, one description? *Atmos. Chem. Phys.* **23**, 10057–10074 (2023).

31. Laaksonen, A., Malila, J. & Nenes, A. Heterogeneous nucleation of water vapor on different types of black carbon particles. *Atmos. Chem. Phys.* **20**, 13579–13589 (2020).

32. Dowell, L. G. & Rinfret, A. P. Low-temperature forms of ice as studied by X-ray diffraction. *Nature* **188**, 1144–1148 (1960).

33. McMillan, J. A. & Los, S. C. Vitreous ice: irreversible transformations during warm-up. *Nature* **206**, 806–807 (1965).

34. Ostwald Wilhelm. Studien über die Bildung und Umwandlung fester Körper. *Z. Phys. Chem.* **22**, 289–332 (1897).

35. Mayer, E. & Hallbrucker, A. Cubic ice from liquid water. *Nature* **325**, 601–602 (1987).

36. Huang, X. et al. Tracking cubic ice at molecular resolution. *Nature* **617**, 86–91 (2023).

37. Wulff, G. Zur Frage der Geschwindigkeit des Wachstums und der Auflösung der Krystallflagen. *Z. Kristallogr.* **34**, 449–530 (1901).

38. Malkin, T. L. et al. Stacking disorder in ice I. *Phys. Chem. Chem. Phys.* **17**, 60–76 (2015).

39. De Yoreo, J. J. et al. Crystallization by particle attachment in synthetic, biogenic, and geologic environments. *Science* **349**, aaa6760 (2015).

40. Ma, X. et al. Tuning crystallization pathways through sequence engineering of biomimetic polymers. *Nat. Mater.* **16**, 767–774 (2017).

41. Niu, H., Yang, Y. I. & Parrinello, M. Temperature Dependence of Homogeneous Nucleation in Ice. *Phys. Rev. Lett.* **122**, 245501 (2019).

42. Avrami, M. Kinetics of phase change. I General theory. *J. Chem. Phys.* **7**, 1103–1112 (1939).

43. Avramov, I. Kinetics of distribution of infections in networks. *Physica A* **379**, 615–620 (2007).

44. Wang, C., Wu, J., Wang, H. & Zhang, Z. Classical nucleation theory of ice nucleation: Second-order corrections to thermodynamic parameters. *J. Chem. Phys.* **154**, 234503 (2021).

45. Haji-Akbari, A. & Debenedetti, P. G. Direct calculation of ice homogeneous nucleation rate for a molecular model of water. *Proc. Natl Acad. Sci. USA* **112**, 10582–10588 (2015).

46. Małolepsza, E. & Keyes, T. Water freezing and ice melting. *J. Chem. Theory Comput.* **11**, 5613–5623 (2015).

47. Vega, C. et al. Heat capacity of water: a signature of nuclear quantum effects. *J. Chem. Phys.* **132**, 046101 (2010).

48. Linstrom, P. & Mallard, W. The NIST Chemistry WebBook: a chemical data resource on the internet. *J. Chem. Eng. Data* **46**, 1059–1063 (2001).

49. Angell, C. A., Shuppert, J. & Tucker, J. C. Anomalous properties of supercooled water. Heat capacity, expansivity, and proton magnetic resonance chemical shift from 0 to -38%. *J. Phys. Chem.* **77**, 3092–3099 (1973).

50. Ickes, L., Welti, A., Hoose, C. & Lohmann, U. Classical nucleation theory of homogeneous freezing of water: thermodynamic and kinetic parameters. *Phys. Chem. Chem. Phys.* **17**, 5514–5537 (2015).

51. Huhtamäki, T., Tian, X., Korhonen, J. T. & Ras, R. H. A. Surface-wetting characterization using contact-angle measurements. *Nat. Protoc.* **13**, 1521–1538 (2018).

52. Zobrist, B., Koop, T., Luo, B. P., Marcolli, C. & Peter, T. Heterogeneous ice nucleation rate coefficient of water droplets coated by a nonadecanol monolayer. *J. Phys. Chem. C* **111**, 2149–2155 (2007).

53. Barahona, D. Thermodynamic derivation of the activation energy for ice nucleation. *Atmos. Chem. Phys.* **15**, 13819–13831 (2015).

54. Thompson, A. P. et al. LAMMPS - a flexible simulation tool for particle-based materials modeling at the atomic, meso, and continuum scales. *Comput. Phys. Commun.* **271**, 108171 (2022).

55. Matsumoto, M., Yagasaki, T. & Tanaka, H. GenIce: hydrogen-disordered ice generator. *J. Comput. Chem.* **39**, 61–64 (2018).

56. Liu, Q.-L. & Priezjev, N. V. The influence of complex thermal treatment on mechanical properties of amorphous materials. *Comput. Mater. Sci.* **161**, 93–98 (2019).

57. Freitas, R., Asta, M. & de Koning, M. Nonequilibrium free-energy calculation of solids using LAMMPS. *Comput. Mater. Sci.* **112**, 333–341 (2016).

58. Frenkel, D. & Ladd, A. J. C. New Monte Carlo method to compute the free energy of arbitrary solids. Application to the fcc and hcp phases of hard spheres. *J. Chem. Phys.* **81**, 3188–3193 (1984).

59. Wang, Z. et al. Source datasets for molecularly resolved mapping of heterogeneous ice nucleation and crystallization pathways using in-situ cryo-TEM. *Figshare* https://doi.org/10.6084/m9.figshare.29400479 (2025).

Acknowledgements

Author contributions

L.W., X.B., L.X., and E.W. conceived and supervised the project. Z.W., Z.Y., M.C., X.H., K.L., Y.W., H.S., L. Liao performed the experiments and calculations. Z.X., W.W., E.W., X.B., and L.W. built the experimental setup. L.X., J.C. and E.W. advised the theoretical modeling. L.Liu advised the sample processing. L.W. and K.L. wrote the paper with contributions from all authors.

Competing interests

The authors declare no competing interests.

Additional information

Supplementary information The online version contains supplementary material available at
https://doi.org/10.1038/s41467-025-62900-w.

Correspondence and requests for materials should be addressed to Xuedong Bai, Limei Xu, Enge Wang or Lifen Wang.

Peer review information *Nature Communications* thanks the anonymous reviewers for their contribution to the peer review of this work. A peer review file is available.

Reprints and permissions information is available at
http://www.nature.com/reprints

Publisher's note Springer Nature remains neutral with regard to jurisdictional claims in published maps and institutional affiliations.